





Frustrated magnetism in octahedra-based $\text{Ce}_6\text{Ni}_6\text{P}_{17}$ D. G. Franco ^{1,2,*} R. Avalos ³ D. Hafner,⁴ K. A. Modic,⁵ Yu. Prots,⁴ O. Stockert,⁴ A. Hoser,⁶
P. J. W. Moll,^{4,7} M. Brando,⁴ A. A. Aligia ^{1,2} and C. Geibel ⁴¹*Centro Atómico Bariloche and Instituto Balseiro - CNEA, 8400 S. C. de Bariloche, Argentina*²*Consejo Nacional de Investigaciones Científicas y Técnicas (CONICET), Argentina*³*Departamento de Física, Colegio de Ciencias e Ingeniería, Universidad San Francisco de Quito, Quito 170901, Ecuador*⁴*Max Planck Institute for Chemical Physics of Solids, D-01187 Dresden, Germany*⁵*Institute of Science and Technology Austria, 3400 Klosterneuburg, Austria*⁶*Helmholtz-Zentrum Berlin für Materialien und Energie, D-14109 Berlin, Germany*⁷*Max Planck Institute for the Structure and Dynamics of Matter, D-22761 Hamburg, Germany*

(Received 28 September 2023; revised 9 January 2024; accepted 16 January 2024; published 5 February 2024)

Magnetic frustration allows to access novel and intriguing properties of magnetic systems and has been explored mainly in planar triangular-like arrays of magnetic ions. In this work, we describe the phosphide $\text{Ce}_6\text{Ni}_6\text{P}_{17}$, where the Ce^{+3} ions accommodate in a body-centered cubic lattice of Ce_6 regular octahedra. From measurements of magnetization, specific heat, and resistivity, we determine a rich phase diagram as a function of temperature and magnetic field in which different magnetic phases are found. Besides clear evidence of magnetic frustration is obtained from entropy analysis. At zero field, a second-order antiferromagnetic transition occurs at $T_{N_1} \approx 1$ K followed by a first-order transition at $T_{N_2} \approx 0.45$ K. With magnetic field new magnetic phases appear, including a weakly first-order transition which ends in a classical critical point and a third magnetic phase. We also study the exact solution of the spin-1/2 Heisenberg model in an octahedron which allows us a qualitative understanding of the phase diagram and compare with the experimental results.

DOI: [10.1103/PhysRevB.109.054405](https://doi.org/10.1103/PhysRevB.109.054405)**I. INTRODUCTION**

Ce-based compounds show a rich variety of magnetic and thermodynamic behaviors, which can be qualitatively understood based on the competition between magnetic order (due to the Ruderman-Kittel-Kasuya-Yosida interaction) and single-ion Kondo physics. Such competition has been rationalized in the so called Doniach phase diagram [1–3], where a tuning parameter, such as magnetic field or pressure, changes drastically the properties of the material. Different behaviors such as heavy-fermion superconductivity, quantum criticality, metamagnetism, among others, have been reported [4–6].

Magnetic frustration has emerged as a new direction to access novel and exotic states of matter in strongly correlated electronic systems [7,8]. It occurs in antiferromagnetic systems when magnetic interactions cannot be satisfied simultaneously, giving rise to non standard ground states where new properties can be found [9–11].

There are two scenarios for the emergence of magnetic frustration. The first one is realized in certain crystalline arrangements: the archetypical example is a triangular lattice with only antiferromagnetic nearest-neighbor interactions. In this case and similar ones, it is not possible to simultaneously align antiferromagnetically all the spins and therefore magnetic frustration arises. Two-dimensional triangular based structures like Kagome and honeycomb lattices have been

studied in this context [11–13]. Also three-dimensional structures are able to show magnetic frustration, for example, the pyrochlore lattice where magnetic ions are arranged in vertex-sharing tetrahedra [7,9,10]. The second scenario is competition between different magnetic interactions, for example nearest-neighbor and next-nearest-neighbor interactions in a square lattice [14,15].

Many insulating frustrated systems have been explored, for example, pyrochlore oxides where fluidlike states of matter can be formed, giving rise to the so called spin-liquid behavior [16]. On the other hand frustrated metallic systems remain largely unexplored. A few examples of intermetallic materials with frustration include the Shastry-Sutherland lattice with magnetic ions arranged on squares with two interactions or triangular-based systems [14,17–19], all of which are two dimensional in nature.

$\text{Ce}_6\text{Ni}_6\text{P}_{17}$ was first synthesized as single crystals at the end of the seventies and crystallizes in the cubic space group $\bar{I}43m$ [20]. This crystal structure is quite unique as it features cerium ions arranged on Ce_6 octahedra on a body-centered cubic unit cell. From the magnetic point of view, six ions arranged in a regular octahedron with antiferromagnetic nearest-neighbor interactions should be frustrated, since each face is an equilateral triangle. Therefore this compound offers the possibility for the study of magnetic frustration on a three-dimensional lattice composed of octahedra. If additional magnetic interactions are important as, for example, next-nearest-neighbor ones, further frustration effects might appear due to competition with these additional magnetic interactions. Indeed,

*diego.franco@cab.cnea.gov.ar

some evidence of frustration was reported [21,22], but the low temperature physical properties were not studied in detail.

In this work, we present the synthesis and characterization of physical properties of polycrystalline and single-crystal $\text{Ce}_6\text{Ni}_6\text{P}_{17}$ by means of magnetization, specific heat, and electrical transport measurements. We show that effectively the system presents a complex phase diagram as a function of temperature and magnetic field, with several magnetic phases where the frustration plays an important role. To provide a theoretical support to experiment, we have solved exactly a spin Heisenberg model for six spins $1/2$ at the vertices of a regular octahedron. The problem is solved in an elegant way using group theory. The effect of interactions between octahedra is also discussed.

The rest of this paper is organized as follows. In Sec. II, we present the details for the synthesis of polycrystalline and single crystal samples and their characterization by means of x-ray and neutron diffraction, magnetization, specific heat, and resistivity. In Sec. III, we present the experimental results, while in Sec. IV, we show the simplified theory for the magnetic interactions. Finally, in Sec. V, we summarize our main results and conclusions.

II. EXPERIMENTAL

Powder samples of $\text{Ce}_6\text{Ni}_6\text{P}_{17}$ and the nonmagnetic analogous compound $\text{La}_6\text{Ni}_6\text{P}_{17}$ were synthesized from Ce/La (Ames Lab), Ni slugs (99.995% Alfa-Aesar), and red P (99.999% Alfa-Aesar) in a three-step procedure. In a first step, the rare-earth (Ce or La) and nickel pieces were melted in an arc melting furnace. The binary alloy was crushed, mixed with red phosphorus in (Ce/La)Ni:P 1:2 molar relation and heated at 700°C for several days in a closed quartz ampule with an aluminum oxide crucible. Slow heating rates were employed in the vicinity of melting and boiling points of P, in order to ease the chemical reaction with the other components. The obtained material was ground to powder, the remaining phosphorus amount to give the desired stoichiometry composition was added and a second heat treatment was performed, similar to the first one.

The initial microscopic mixture of cerium and nickel metals by arc melting, as well as the reaction with phosphorus in two stages, were necessary steps to reduce the reaction time and the loss of phosphorus. It is important to notice that the 6-6-17 stoichiometry implies a high phosphorus to metal ratio.

$\text{Ce}_6\text{Ni}_6\text{P}_{17}$ single crystals were grown in tin flux. The overall composition Ce:Ni:P:Sn was 1:1:8:30. The mixture was placed in an alumina crucible and heated in a quartz ampule up to 900°C in order to dissolve all solutes. After an initial fast cooling to 750°C , the temperature was slowly decreased to 400°C at $0.03^\circ\text{C}/\text{min}$, and then the furnace was cooled down to room temperature. The single crystals were obtained dissolving the flux with diluted HCl. Typically $\text{Ce}_6\text{Ni}_6\text{P}_{17}$ crystals were approximately $0.20\text{ mm} \times 0.20\text{ mm} \times 0.20\text{ mm}$ in size.

Chemical composition on all samples was confirmed by energy-dispersive x-ray spectroscopy (SEM-EDX, Zeiss Crossbeam 340). Powder x-ray diffraction patterns (XRD) were measured at room temperature on a STOE Stadip MP instrument with $\text{Cu K}\alpha_1$ radiation ($\lambda = 1.54056\text{ \AA}$). Single-

crystal data for the cerium compound only were collected on a Rigaku AFC7 diffractometer, Saturn 724+ CCD detector with $\text{Mo K}\alpha$ radiation. Neutron powder diffraction patterns (NPD) at several temperatures were measured on a $\text{Ce}_6\text{Ni}_6\text{P}_{17}$ powder sample at the E6 diffractometer, HZB facility, $\lambda = 2.43\text{ \AA}$. Crystal structure refinements were done in the powder data case with FULLPROF program [23] and in single crystal data with SHELXL [24]. The crystal structure was drawn using VESTA [25].

Magnetization (M) was measured as a function of temperature ($1.8 < T < 300\text{ K}$) and magnetic field (H) in a Quantum Design SQUID VSM - 70 kOe magnetometer. A ^3He attachment to a Quantum Design SQUID MPMS - 70 kOe magnetometer was used for low temperature measurements ($0.5 < T < 2\text{ K}$). Specific heat (C) measurements on polycrystalline samples were performed in a Quantum Design PPMS system with a ^3He option up to 70 kOe by the standard two-tau model and also with a single slope analysis of relaxation curves. $\text{La}_6\text{Ni}_6\text{P}_{17}$ was used as the nonmagnetic analog for phonon and electronic specific heat subtraction. Temperature and field dependencies of the resistance (R) were measured on focused ion beam (FIB) microstructures prepared from $\text{Ce}_6\text{Ni}_6\text{P}_{17}$ single crystals with a conventional four-probe configuration. The small crystals were fabricated into microbars to facilitate homogeneous current flow and a reliable determination of the resistivity, following the recipe of Ref. [26]. A Quantum Design PPMS system with ^3He option and an Oxford K400 dilution refrigerator were used. Resistivity was measured along [110] crystallographic direction with the applied magnetic field in the direction of the electrical current.

III. EXPERIMENTAL RESULTS

A. Synthesis and diffraction

High-purity polycrystalline $\text{La}_6\text{Ni}_6\text{P}_{17}$ and $\text{Ce}_6\text{Ni}_6\text{P}_{17}$ samples were obtained as confirmed by x-ray powder diffraction data. Besides small $\text{Ce}_6\text{Ni}_6\text{P}_{17}$ single crystals were grown in tin flux. Homogeneous distribution of Ce, Ni, and P atoms as well as the expected Ce:Ni:P 6:6:17 stoichiometry was verified by energy-dispersive x-ray spectroscopy. A typical spectra together with atomic distribution maps can be found in Ref. [27].

Cerium and lanthanum compounds crystallize in the cubic space group $\bar{I}43m$. Lattice parameters and xyz positions are shown in Table I and are in good agreement with previous reports on these materials [20]. The Rietveld refinement of the x-ray room temperature data for the cerium compound is shown in the top panel of Fig. 1. Crystal structure refinement results for $\text{Ce}_6\text{Ni}_6\text{P}_{17}$ single-crystal data are available on the joint CCDC/FIZ Karlsruhe deposition service, CSD 2296485 [28]. The rare-earth (RE) ion in this crystal structure is located at a $12e$ site with C_{2v} symmetry giving a body-centered cubic arrangement of RE_6 octahedra, as shown schematically in Fig. 2. A given RE ion has four nearest-neighbors (NN) in the same octahedra, red bonds in the figure, one next-nearest neighbor (NNN) in an adjacent octahedra, blue, and one next-next-nearest neighbor (NNNN) on the opposite side of the same octahedra, yellow. For the cerium compound the

TABLE I. Crystal structure for $\text{Ce}_6\text{Ni}_6\text{P}_{17}$ [$a = 10.11490(9)$ Å] and $\text{La}_6\text{Ni}_6\text{P}_{17}$ [$a = 10.17433(9)$ Å], space group $I\bar{4}3m$, $Z = 2$. The results were obtained from refinement on powder samples (pc) and single crystal (sc) x-ray diffraction data. Agreement factors are also shown.

	Atom	Site	x	y	z
$\text{La}_6\text{Ni}_6\text{P}_{17}$ pc	La	12e	0.2894(1)	0	0
	Ni	12d	1/4	1/2	0
	P1	24g	0.2027(3)	x	0.4320(4)
	P2	8c	0.2121(4)	x	x
	P3	2a	0	0	0
$\chi^2 = 4.82, R_B = 0.175, R_f = 0.113$					
$\text{Ce}_6\text{Ni}_6\text{P}_{17}$ pc	Ce	12e	0.28932(9)	0	0
	Ni	12d	1/4	1/2	0
	P1	24g	0.2021(2)	x	0.4326(3)
	P2	8c	0.2131(3)	x	x
	P3	2a	0	0	0
$\chi^2 = 2.04, R_B = 0.0234, R_f = 0.0196$					
$\text{Ce}_6\text{Ni}_6\text{P}_{17}$ sc	Ce	12e	0.28927(3)	0	0
	Ni	12d	1/4	1/2	0
	P1	24g	0.20207(8)	x	0.4323(1)
	P2	8c	0.2135(1)	x	x
	P3	2a	0	0	0
$R1 = 0.0216, wR2 = 0.0449$					

following distances were obtained: ≈ 4.138 , ≈ 4.261 , and ≈ 5.852 Å for NN, NNN, and NNNN, respectively. Similar distances were found for the lanthanum compound.

To characterize possible changes in the crystal structure and magnetic ordering at low temperatures in $\text{Ce}_6\text{Ni}_6\text{P}_{17}$, we measured neutron powder diffraction (NPD) from room temperature down to 0.245 K. We show in the lower panel of Fig. 1 some selected diffractograms for $T \lesssim 90$ K. Neither additional peaks nor splitting in the reflections is observed down to 0.245 K disregarding a change in the cubic $I\bar{4}3m$ crystal structure. The evolution of the cell parameter with temperature is shown in the inset, where a typical contraction on cooling is obtained. Besides no long-range magnetic order is observed on the neutron data. However we will show next clear evidence in magnetization, specific heat, and resistivity data, that there is magnetic order below 1 K. This apparent contradiction is explained based on the nature of the ground state for $\text{Ce}_6\text{Ni}_6\text{P}_{17}$ and will be fully derived and explained in Sec. IV. Essentially the ground state is, according to our model, a singlet and therefore the system is in a nonmagnetic state. As a consequence no magnetic neutron diffraction is expected.

B. Magnetization

At 10kOe a Curie-Weiss $M/H = C/(T - \Theta_{\text{CW}})$ behavior was found above 200 K, Fig. 3 top panel, where C is the Curie constant and Θ_{CW} the Curie-Weiss temperature. The effective magnetic moment $\mu_{\text{eff}} = 2.52(4)\mu_B$, calculated from C , is in good agreement with the expected value according Hund's rules for a Ce^{+3} ion with $J = 5/2$: $\mu_{\text{eff}}(\text{Ce}^{+3}) = 2.54(4)\mu_B$. The obtained Curie-Weiss temperature is $\Theta_{\text{CW}} =$

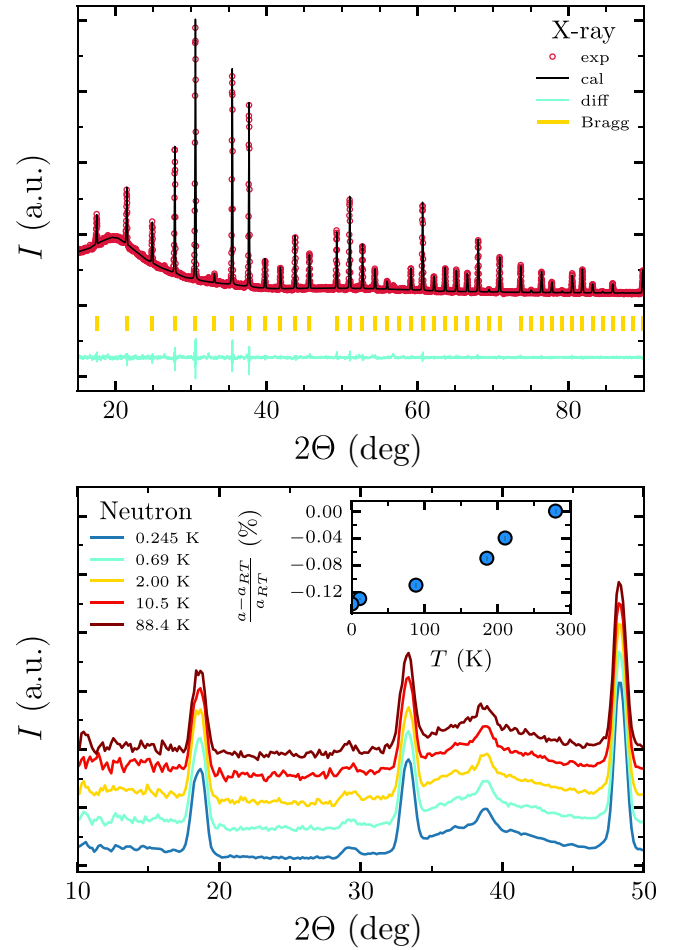


FIG. 1. Powder diffraction data for $\text{Ce}_6\text{Ni}_6\text{P}_{17}$. (Top) Rietveld refinement of XRD data in the cubic $I\bar{4}3m$ space group (Cu $K_{\alpha 1}$, $\lambda = 1.54056$ Å). (Bottom) NPD at low temperatures as indicated, $\lambda = 2.43$ Å. The diffractogram at 0.245 K does not display additional Bragg peaks connected with antiferromagnetic order. The inset shows the relative thermal evolution of the cell parameter a ; a_{RT} is the cell parameter at room temperature. Error bars are smaller than the symbols used.

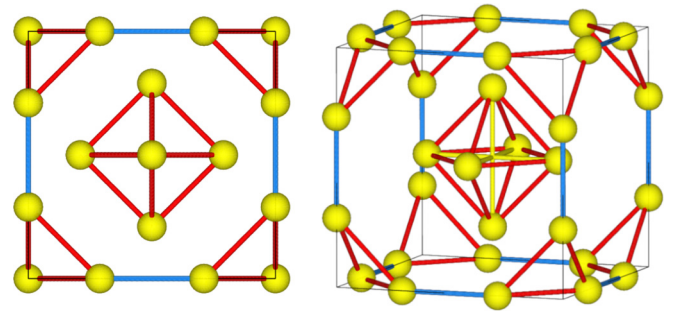


FIG. 2. Two views of $\text{RE}_6\text{Ni}_6\text{P}_{17}$ cubic unit cell (black line), space group $I\bar{4}3m$, showing RE subcell as yellow spheres. NN, NNN, and NNNN interactions are shown as red, blue and yellow bonds respectively. A body-centered cubic lattice of RE_6 octahedra is recognized identifying the octahedra formed by the RE yellow spheres joined by red lines.

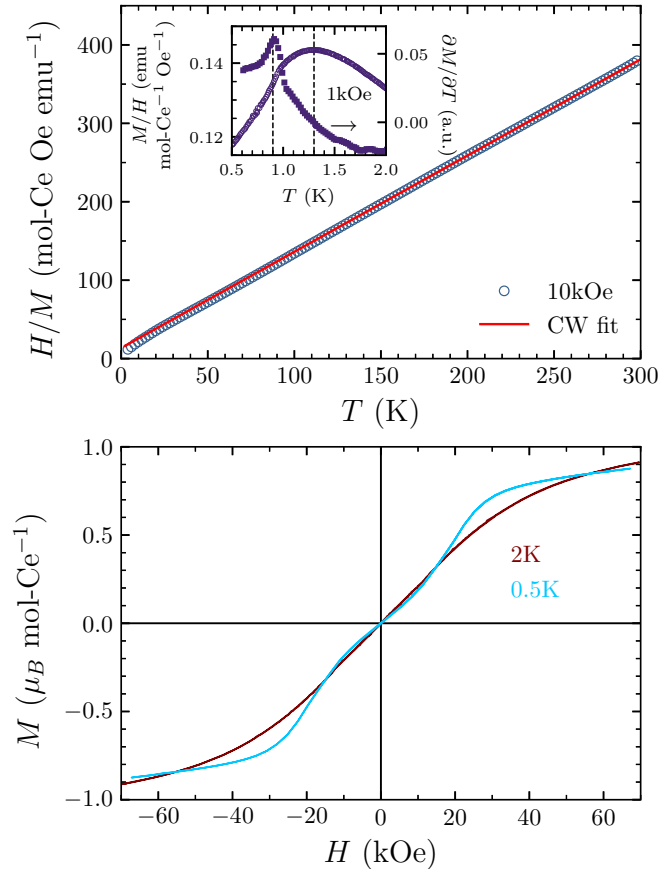


FIG. 3. Magnetization measurements for a powder $\text{Ce}_6\text{Ni}_6\text{P}_{17}$ sample. (Top) Temperature (T) dependence of H/M at 10 kOe (dots). The red line represents a Curie-Weiss fit above 200 K. The inset shows the low-temperature magnetization at 1 kOe (left axis) and the temperature derivative of magnetization (right axis). The vertical striped lines indicate the maximum (zero) and inflection point (maximum) in the magnetization (temperature derivative of magnetization) which correspond to T_m and T_{N_1} , respectively. (Bottom) M vs H at 2 and 0.5 K.

–11 K, which indicates predominantly antiferromagnetic interactions between cerium ions. Similar μ_{eff} and Θ_{CW} values were obtained from data measured at 1 and 70 kOe (data not shown).

At low temperatures, no peak typical for a long range antiferromagnet is observed, see inset in Fig. 3 for 1 kOe magnetization data, but a broad cusp with a maximum at $T_m = 1.15$ K (1.30 K) and an inflection point at 0.80 K (0.90 K) at 10 kOe (1 kOe). This temperature dependence of the magnetization closely resembles the behavior in CePdAl and $\text{Yb}_2\text{Pt}_2\text{Pb}$, two known frustrated metallic compounds [17,29–31]. The inflection point obtained for $\text{Ce}_6\text{Ni}_6\text{P}_{17}$ is a characteristic temperature for a phase transition to an antiferromagnetic state and therefore we call it T_{N_1} . On the other hand, T_m characterizes the broad maximum and reflects magnetic fluctuations above the ordering temperature. Further data and analysis supporting magnetic transitions in this compound will be presented when discussing specific heat and resistivity measurements, see below. High values of the empirical ratio $f_{\text{CW}} = |\Theta_{\text{CW}}|/T_N$ have been used mainly in insulating systems as a measure of frustration, as magnetic

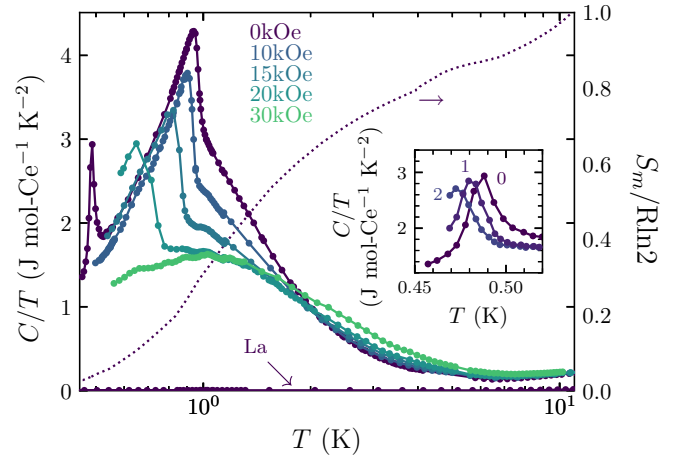


FIG. 4. C/T at different magnetic fields for a powder $\text{Ce}_6\text{Ni}_6\text{P}_{17}$ sample. $\text{La}_6\text{Ni}_6\text{P}_{17}$ nonmagnetic analog is also shown at zero applied magnetic field (La). The dotted line is the $\text{Ce}_6\text{Ni}_6\text{P}_{17}$ magnetic entropy (for $H = 0$ kOe), to be read on the right axis. A detail of C/T around T_{N_2} for small fields (in kOe) is plotted in the inset.

systems with no frustration order at approximately the same energy scale as given by Θ_{CW} and therefore $|\Theta_{\text{CW}}| \approx T_N$ [32]. For metallic systems, a more appropriate ratio is $f = T_m/T_N$, where T_m plays the role of energy scale as it reflects the ordering temperature for the system without frustration. For $\text{Ce}_6\text{Ni}_6\text{P}_{17}$, taking $T_N = T_{N_1} = 0.90$ K and $T_m = 1.30$ K, one obtains $f = 1.44$, similar to the value 1.5 reported in frustrated systems like CePdAl [17] and the Shastry-Sutherland lattice $\text{Yb}_2\text{Pt}_2\text{Pb}$ [31]. In no frustrated systems $f = 1$ because there is no difference between T_N and T_m .

The field dependence of the magnetization at 2 K, Fig. 3 bottom panel, shows a paramagnetic-like behavior with a tendency to saturation at about $1\mu_B$ at 70 kOe. At 0.5 K, a feature like a broadened step appears at about 20.5 kOe, resembling a metamagnetic-like transition between two different magnetic states. No hysteresis is observed.

C. Specific heat

Figure 4 shows the main specific heat C/T versus T results below 10 K where several features are observed. First a clear peak is seen at $T_{N_1} \approx 1$ K for zero applied magnetic field. This temperature correlates with the inflection point previously discussed on magnetization versus temperature data, see inset in Fig. 3. Besides there is a second peak which corresponds to another magnetic transition at $T_{N_2} \approx 0.5$ K. Taking into account that no secondary phases were detected by x-ray diffraction and the bulk nature of the specific heat technique we can safely disregard an impurity contribution to the obtained data and consider both peaks as bulk magnetic transitions for $\text{Ce}_6\text{Ni}_6\text{P}_{17}$. The relatively small anomaly in C versus T at T_{N_1} is compensated by a large tail extending far above the transition temperature. This large tail and the broad maximum in M/H for $T > T_{N_1}$ indicate strong fluctuations above the ordering temperature as a consequence of magnetic frustration. The effect of the magnetic field is to shift both specific heat peaks to lower temperatures, as expected for an antiferromagnet. At high fields, where the magnetic

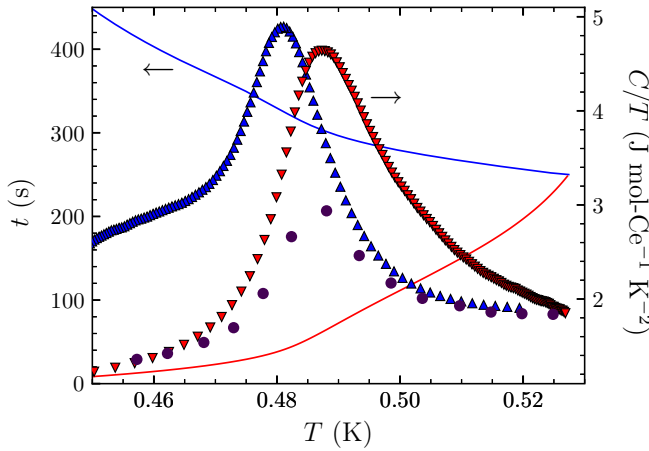


FIG. 5. Heat pulse (left axis, lines) and specific heat (right axis, symbols) of $\text{Ce}_6\text{Ni}_6\text{P}_{17}$ around T_{N_2} and zero magnetic field. Warming and cooling parts of the heat pulse (red and blue lines, respectively) show a subtle indication of a first-order phase transition at T_{N_2} . Specific heat data obtained from a single slope analysis of the warming and cooling part of the heat pulse are shown as red and blue triangles, respectively. For comparison, the values measured with the conventional thermal relaxation technique are shown as violet circles.

order is suppressed, a Schottky-like dependence typical for a completely polarized state emerges and shifts to higher temperatures as the field is increased.

The data just described were obtained with the standard two-tau model measurement protocol of the PPMS system [33], which consists of heating-cooling cycles initiated by a heat pulse. When the specific heat does not depend strongly on temperature, a single specific heat value can be obtained fitting the complete temperature versus time relaxation curve of one pulse with a model that takes into account the relaxation of the sample with the sample platform [34]. For getting the temperature dependence of the specific heat, several pulses at different base temperature are needed.

When the specific heat changes appreciably with temperature or there is a transition with latent heat (as in first-order phase transitions), this approach is not adequate; instead a single slope analysis is recommended. This second method uses a unique relaxation curve for getting the specific heat values between the maximum and minimum temperature of the relaxation curve. A detailed discussion and analysis on this matter can be found in Ref. [35] and references therein.

Figure 5 shows a typical time versus temperature heat pulse in the vicinity of T_{N_2} where a clear change in slope is seen on both parts of the heat pulse (heating and cooling), suggesting a first-order nature of the magnetic transition. This feature is not taken into account on the standard two-tau model and therefore a single slope analysis was performed. On the right axis of Fig. 5, the obtained specific heat is plotted revealing a small hysteresis of about 7 mK between heating and cooling curves. Further evidence of the first-order nature of the transition at T_{N_2} was obtained also in resistivity data (see next section). For comparison the specific heat measured with the standard protocol is also shown on the figure, demonstrating a clear underestimation of the specific heat values. The heat pulses around T_{N_1} do not show any change in slope and the two-tau model was good enough to fit the data.

The measured specific heat C at zero applied magnetic field can be decomposed in three different contributions: $C = C_{\text{mag}} + C_{\text{el}} + C_{\text{ph}}$, where C_{mag} , C_{el} , and C_{ph} stand for the magnetic, electron, and phonon contributions respectively to the total specific heat of the sample. In order to obtain C_{mag} , it is necessary to subtract C_{el} and C_{ph} . With that aim we measured the specific heat on the isostructural nonmagnetic compound $\text{La}_6\text{Ni}_6\text{P}_{17}$, see Fig. 4. It is clear that the electronic and phonon contributions are practically negligible in comparison with the magnetic specific heat. With C_{mag} we calculated the magnetic entropy S_m as $S_m(T) = \int C_{\text{mag}}/T dT$, see Fig. 4. For Ce^{+3} in a doublet ground state, the entropy should reach $S_m(\infty) = R\ln 2$ at saturation. In magnetic systems where there is no magnetic frustration, the expected value at the transition temperature is $S_m(T_N) \approx 0.9S_m(\infty)$. Experimental results show that a huge amount of entropy is missing at T_{N_1} , as $S_m(T_{N_1}) \approx 0.35S_m(\infty)$. The remaining entropy is recovered well above the ordering temperature and S_m tends to the expected value around 10 K, reflecting the experimental tail observed in C versus T . This indication of strong fluctuations and entropy accumulation above the phase-transition temperature hints to a strong degree of magnetic frustration on the system [36].

D. Electronic transport

The magneto electronic transport properties were measured on microstructured lamella cut from $\text{Ce}_6\text{Ni}_6\text{P}_{17}$ single crystals. Such FIB-machining not only allows an exceptional control over shape, size and contact alignment, but also eliminates possible surface impurity remains from the growing process. Figure 6 shows the temperature and field dependence of resistivity measured with the magnetic field applied parallel to the direction of the electrical current. The residual resistivity ratio calculated as R_{RT}/R_{LT} , where RT is room temperature and LT is low temperature corresponding to approximately 0.4 K, is around 70 for [110] direction. This value indicates a high crystalline quality with small amounts of defects and impurities. While small differences between the absolute values of the measured resistivity for different crystalline directions and field and current configurations (perpendicular or parallel) were observed, the main features associated with magnetic transitions and changes in behavior that we will discuss remain unaffected by such different measurement conditions.

The temperature dependence of resistivity clearly shows a metallic like behavior with no evidence of Kondo effect, see upper inset in the upper panel of Fig. 6. At about 10 K, there is clear change in regime reflecting the onset of magnetic fluctuations, followed by a kink at $T_{N_1} = 0.96$ K and a steplike transition at $T_{N_2} = 0.44$ K. The applied magnetic field shifts both magnetic transitions to lower temperatures. These evidences are in good correlation with specific heat results previously discussed. At high fields a quadratic dependence $\rho(T)$ is observed, as expected according to Fermi-liquid theory.

Figure 6 lower panel shows field scans of resistivity at selected temperatures, sweeping the field up and down, where several features are observed. On one hand, at the highest temperature (900 mK), there is a maximum which corresponds with T_{N_1} . The decrease of temperature shifts T_{N_1} to

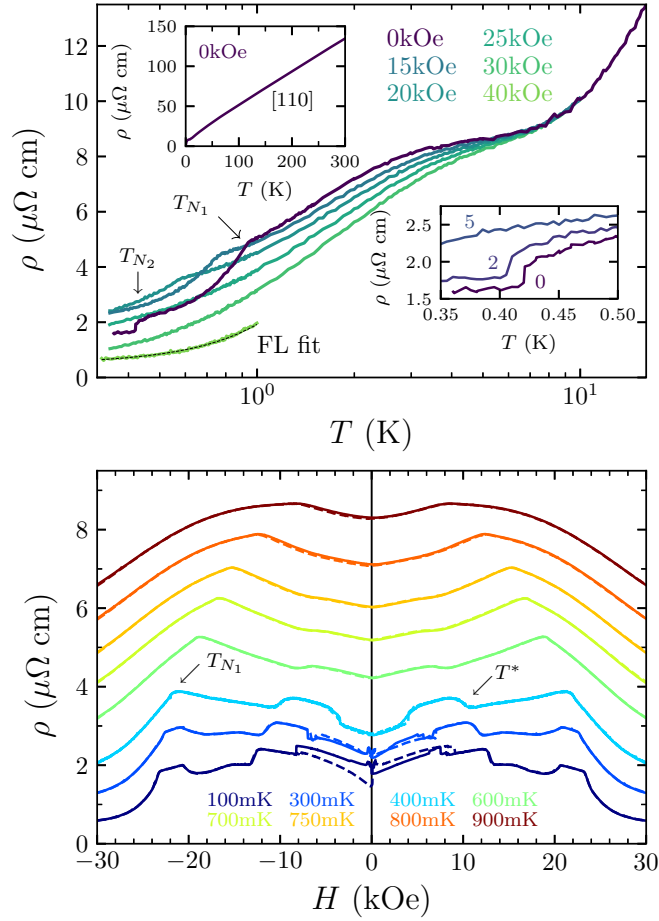


FIG. 6. Magneto electronic transport measurements on a $\text{Ce}_6\text{Ni}_6\text{P}_{17}$ single crystal. (Top) ρ vs T at different constant applied magnetic fields H along the [110] crystalline direction. For $H = 40$ kOe, a Fermi-liquid (FL) fit is shown as a dashed line. The upper inset shows the resistivity at zero field from room temperature down to ≈ 0.4 K. The lower inset shows a zoom on the low temperature region for small fields: 0, 2, and 5 kOe. (Bottom) ρ vs H at constant temperature. Curves obtained sweeping the field up and down are shown for all cases by continuous and dashed lines, respectively. Measurements were displaced by $0.6\mu\Omega$ cm with respect to each other for clarity, except 100-mK data.

higher fields and at 300 mK—and lower temperatures—it splits in two separate kinks indicating the emergence of a new magnetic phase. On the other hand, at the lowest temperature and low fields a hysteresis between up and down field sweeps is clearly observed. This demonstrates without doubt the first-order nature of the magnetic transition occurring at T_{N_2} , validating the evidence already seen and discussed on specific heat measurements. There is a further feature in the field dependence of resistivity below 800 mK. We define the characteristic temperature for this change in the electrical behavior by T^* , taken as the inflection point on $\rho(H)$.

E. Magnetic phase diagram

Characteristic magnetic transitions for $\text{Ce}_6\text{Ni}_6\text{P}_{17}$ obtained from magnetization, specific heat, and resistivity data are collected on the magnetic phase diagram T - H shown in Fig. 7.

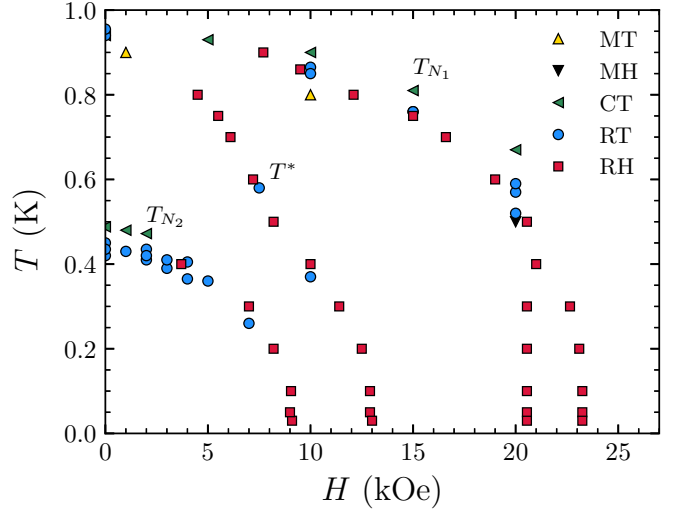


FIG. 7. Magnetic phase diagram T - H obtained from temperature and field dependence of magnetization (MT and MH, respectively), specific heat data (CT), and temperature and field dependencies of resistivity (RT and RH, respectively) on $\text{Ce}_6\text{Ni}_6\text{P}_{17}$.

Except for small differences coming from different techniques on different instruments there is a clear agreement on the magnetic behavior of the compound. A monotonous decrease of the characteristic temperatures T_{N_1} and T_{N_2} is seen when increasing the applied magnetic field, with the appearance of a new magnetic phase below 400 mK and fields approximately between 20.5 and 23 kOe.

On the other hand, T^* seems to be a weakly first-order phase transition which ends in a classical critical end point at $T \approx 800$ mK, resulting in a crossover behavior for $T > 800$ mK. This has been confirmed by $\rho(H)$ curves measured at 860 and 900 mK, where no kink is observed around the expected value for T^* . We note that in another system, a similar signature in magnetoresistance to the one observed at T^* have been reported [37]. Such feature is accompanied with jumps in the field dependence of magnetization and do not correspond to real phase transitions but to reorientation of magnetic domains [38]. In our system no jump in $M(H)$ at 0.5 K is observed around 8 kOe, see Fig. 3, disregarding a domain reorientation. We will return to the nature of this T^* line when discussing the crossovers as a function of magnetic field in Sec. IV D.

IV. SIMPLIFIED THEORY FOR THE MAGNETIC INTERACTIONS IN $\text{Ce}_6\text{Ni}_6\text{P}_{17}$

The evolution of the entropy with temperature indicates that the Ce^{+3} ions have a doublet ground state, in agreement with the physical expectations for an isolated cerium ion in an environment with C_{2v} symmetry. Our main approximation is to assume that the magnetic properties of the system can be described by an isotropic Heisenberg model for the spins of a basic Ce_6 octahedron. Thus the essential part of the Hamiltonian has the form

$$H_{\text{Heis}} = J_1 \sum_{\langle i,j \rangle} \mathbf{S}_i \cdot \mathbf{S}_j + J_2 \sum_{\langle\langle i,j \rangle\rangle} \mathbf{S}_i \cdot \mathbf{S}_j, \quad (1)$$

where (i, j) indicates nearest neighbors (edges of the octahedron, red bonds in Fig. 2) and $\langle\langle i, j \rangle\rangle$ next next-nearest neighbors (opposite sites of the octahedron, yellow bonds in Fig. 2). In the real system, one expects that the interactions are more involved and depend on the structure of the ground-state doublet determined by the crystal-field felt by both interacting Ce atoms. A limiting case would be like the spin Kitaev model, in which for a bond in the direction of the unit vector \hat{v} , the interaction has the form $(\mathbf{S}_i \cdot \hat{v})(\mathbf{S}_j \cdot \hat{v})$ [39]. However, the detailed structure of the doublet is not known and therefore we assume isotropic interactions. As it will be shown next, such simplified model with only a small cluster of six sites in a regular octahedron is able to explain and describe most of the experimental features observed.

A shortcoming of the model in Eq. (1) is that for total spin of the octahedron $S = 2$ and 3, the degeneracy $2S + 1$ is too large for the cubic symmetry of the octahedron. Therefore we have added to the Hamiltonian a cubic crystal field, which corresponds to include the expansion up to fourth order in spin components in O_h symmetry [40]

$$H_{CF} = C \left\{ 35S_z^4 + \frac{5}{2}(S_+^4 + S_-^4) - [30S(S+1) - 25]S_z^2 - 6S(S+1) + 3S^2(S+1)^2 \right\}, \quad (2)$$

where S_z is the total spin projection of the octahedron and S_+ and S_- are the raising and lowering spin operators, respectively.

Including a magnetic field, the Hamiltonian takes the form

$$H = H_{\text{Heis}} + H_{CF} - BS_z, \quad (3)$$

where $B = g\mu_B H$, g is the gyromagnetic factor and μ_B the Bohr magneton.

An important term missing in H is the magnetic interaction between different Ce_6 octahedra. We left this out because the simplest assumption for the magnetic ordering of the system, that all six spins of each octahedron are oriented in the same direction, needs too strong interactions to lead to long-range magnetic order. We return to this point below.

A. Solution of the Heisenberg Hamiltonian

The Hamiltonian (1) has the property that it is invariant under the operations of the point group O_h applied to the space part (the six positions of the spins) keeping the spins fixed, and also the symmetry operations of $\text{SU}(2)$ for the total spin. Therefore it can be solved in an elegant way constructing the states for each given total spin S and spin projection S_z that for the space part have a well defined symmetry. Specifically, for each S, S_z , we project the space part over the basis states of the irreducible representations of the symmetry point group O_h . The general procedure and the matrices used can be found in Ref. [41].

Although there are $2^6 = 64$ states in the system, using symmetry the largest matrices that have to be solved are 2×2 (one for $S = 0$ and irreducible representation A_{2u} and another one for $S = 1$ and T_{1u}). The resulting energies classified by total spin and irreducible representation are listed in Table II.

The degeneracy of each eigenstate is given by $(2S + 1)d$ where d is the dimension of the irreducible representation (irrep) of the space part, which is 1 for the A , 2 for E , and

TABLE II. Energies of the Heisenberg model Eq. (1) for different total spin and irreducible representations (irrep).

S	irrep	E_{Heis}
0	A_{2u}	$-3J_1 + \frac{3}{4}J_2$
0	T_{2u}	$-2J_1 - \frac{1}{4}J_2$
0	A_{2u}	$-\frac{9}{4}J_2$
1	A_{1g}	$-2J_1 + \frac{3}{4}J_2$
1	E_u	$-2J_1 + \frac{3}{4}J_2$
1	T_{1u}	$-J_1 - \frac{1}{4}J_2$
1	T_{1u}	$-\frac{5}{4}J_2$
2	E_u	$\frac{3}{4}J_2$
2	T_{2u}	$J_1 - \frac{1}{4}J_2$
3	A_{1g}	$3J_1 + \frac{3}{4}J_2$

3 for T independently of the subscript which indicates the symmetry under inversion (g for even and u for odd states). For the particular case $J_2 = J_1$, the symmetry increases to the permutation group of six elements S_6 and there are additional degeneracies.

From the resulting energies, it is easy to realize that neglecting H_{CF} and assuming not too large J_2 , in particular for $|J_2| \leq J_1$, the model predicts three transitions at temperature $T = 0$ as a function of magnetic field between the state of minimum energy for $S = i - 1$ and $S = i$ at the critical fields

$$B_i = iJ_1. \quad (4)$$

Remarkably, this simple result is independent of J_2 in the indicated range. We also obtain that other results do not change substantially with J_2 . Therefore we will take $J_2 = 0$ in the numerical evaluations shown here.

Experimentally there are four transitions as a function of magnetic field for $T = 0$, see Fig. 7. In fact, we find that splitting the states of $S = 2$ and 3 by the cubic crystal field given by Eq. (2), for certain values of the factor C , five states appear in the ground state for increasing B giving rise to four transitions.

B. The structure of the ground state

For small J_2 and B , among the 20 spin configurations with $S_z = 0$, 12 are present (with equal probability) in the ground state, which has total spin $S = 0$ and space symmetry A_{2u} . The remaining eight configurations are present in the excited state with $S = 0$ and space symmetry A_{2u} . The state of smallest energy, the ground state, can be constructed combining two spin triplets to form a total spin 0 (a singlet). One of the triplet is constructed from two spins at opposite sites of the octahedron, which we call the ‘‘poles’’:

$$\begin{aligned} |11\rangle_P &= |\uparrow\uparrow\rangle, & |10\rangle_P &= \frac{|\uparrow\downarrow\rangle + |\downarrow\uparrow\rangle}{\sqrt{2}}, \\ |1-1\rangle_P &= |\downarrow\downarrow\rangle. \end{aligned} \quad (5)$$

TABLE III. Energies of the crystal field plus magnetic field term $H_{\text{CF}} - BS_z$ for different total spin and eigenvalues of a rotation in $\pi/2$.

S	C_4	E_2
2	1	$72C$
2	$-i$	$-48C - B$
2	i	$-48C + B$
2	-1	$12C - \sqrt{(2B)^2 + (60C)^2}$
2	-1	$12C + \sqrt{(2B)^2 + (60C)^2}$
3	1	$120C$
3	$-i$	$120C + B - \sqrt{(2B + 60C)^2 + 240C^2}$
3	$-i$	$120C + B + \sqrt{(2B + 60C)^2 + 240C^2}$
3	i	$120C - B - \sqrt{(2B - 60C)^2 + 240C^2}$
3	i	$120C - B + \sqrt{(2B - 60C)^2 + 240C^2}$
3	-1	$-420C - \sqrt{(2B)^2 + (300C)^2}$
3	-1	$-420C + \sqrt{(2B)^2 + (300C)^2}$

The remaining spins at the ‘‘equator’’ ordered in a ring of four sites constitute the other spin triplet:

$$\begin{aligned}
 |11\rangle_E &= \frac{1}{2}(-|\downarrow \uparrow \uparrow \uparrow\rangle + |\uparrow \downarrow \downarrow \downarrow\rangle - |\uparrow \uparrow \downarrow \downarrow\rangle + |\uparrow \uparrow \downarrow \downarrow\rangle), \\
 |1-1\rangle_E &= \frac{1}{2}(|\uparrow \downarrow \downarrow \downarrow\rangle - |\downarrow \uparrow \downarrow \downarrow\rangle + |\downarrow \downarrow \uparrow \downarrow\rangle - |\downarrow \downarrow \downarrow \uparrow\rangle), \\
 |10\rangle_E &= \frac{1}{\sqrt{2}}(|\uparrow \downarrow \uparrow \downarrow\rangle - |\downarrow \uparrow \downarrow \uparrow\rangle).
 \end{aligned} \quad (6)$$

The ground state is

$$\begin{aligned}
 |g\rangle &= \frac{1}{\sqrt{3}}(|11\rangle_P \otimes |1-1\rangle_E - |10\rangle_P \otimes |10\rangle_E \\
 &\quad + |1-1\rangle_P \otimes |11\rangle_E).
 \end{aligned} \quad (7)$$

It is important to stress that the ground state is a singlet and it has a substantial energy gap with the excited triplet. As a consequence, for zero applied magnetic field, one expects a nonmagnetic system. Such scenario explains the lack of magnetic peaks in the neutron diffraction experiments discussed in Sec. III A.

C. Splitting of the spin degeneracy by the cubic crystal field

The energy for each eigenstate of the Hamiltonian $|j\rangle$ is given by

$$E(j) = E_{\text{Heis}}(j) + E_2(j), \quad (8)$$

where $E_{\text{Heis}}(j)$ is given in Table II and $E_2(j)$ is the contribution to the energy of $H_{\text{CF}} - BS_z$ [last two terms of Eq. (3)]. For the states with $S = 0$, $E_2(j) = 0$, and for the states with $S = 1$, $E_2(j) = -BS_z$, since the crystal field does not split these states. For $S = 2$ and 3, we extend the results of Lea, Leask, and Wolf [40] to the case when a magnetic field is present. The corresponding energies are listed in Table III.

Each eigenstate is also eigenstate of the operator \hat{C}_4 of a rotation of the spin in $\pi/2$ around z : $\hat{C}_4|j, S\rangle = C_4|j, S\rangle$, where $|j, S\rangle$ is the spin part of the eigenstate $|j\rangle$. The eigenvalues

TABLE IV. Magnetic fields at which a transition occur B_T/J_1 and the spin projection before transition $\langle S_z \rangle_o$ and after transition $\langle S_z \rangle_f$.

B_T/J_1	$\langle S_z \rangle_o$	$\langle S_z \rangle_f$
1	0	1
1.856	1	1.778
3.540	1.931	1.997
3.936	1.997	2.962

$C_4 = \exp(-i\pi S_z/2)$ are listed in the table. The expectation value is $\langle j|S_z|j\rangle = -\partial E_2(j)/\partial B$.

Choosing $C = 0.00638J_1$ and $J_2 = 0$, we obtain four transitions as a function of magnetic field at zero temperature in qualitative agreement with experimental results. The first one corresponds to $B_1 = J_1$ (as for $C = 0$) between the state of lowest energy with $S = 0$ and space symmetry A_{2u} and the degenerate states with $S = S_z = 1$ and space symmetry A_{1g} and E_u . The second transition at $B_2 = 1.856J_1$ is between the latter state and the state of lowest energy with $S = 3$, space symmetry A_{1g} and $C_4 = -1$. The third transition at $B_3 = 3.540J_1$ takes place between the latter state and the state of lowest energy with $S = 2$, space symmetry E_u and $C_4 = -1$. Finally the last transition at $B_4 = 3.936J_1$ corresponds to the transition between the latter state and the state of lowest energy with $S = 3$, space symmetry A_{1g} and $C_4 = i$.

The expectation value of the total spin projection of the octahedron $\langle S_z \rangle$ as a function of magnetic field is like a staircase with four jumps at the transition points B_i . The values B_i and $\langle S_z \rangle$ at the transitions are listed in Table IV.

D. Crossovers as a function of magnetic field at finite temperature

For finite T , the total spin projection of the octahedron $\langle S_z \rangle$ as a function of B is a continuous smooth function, see Fig. 8. Therefore the transitions described at the end of the previous section become crossovers. We expect that

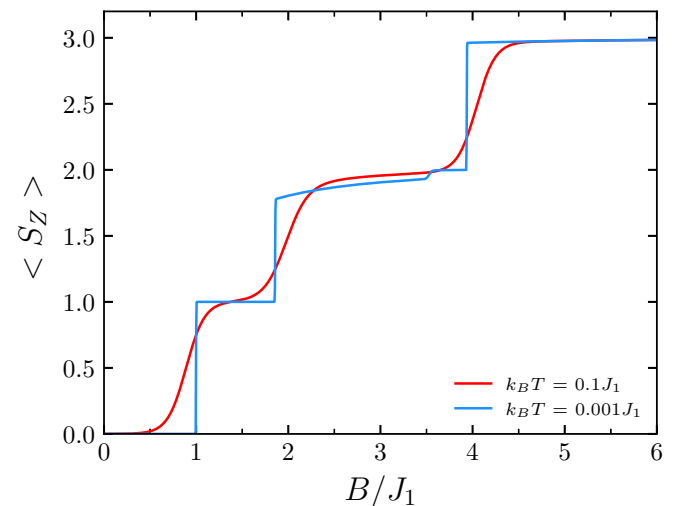


FIG. 8. Spin projection $\langle S_z \rangle$ as a function of magnetic field B at different temperatures and $C = 0.00638J_1$.

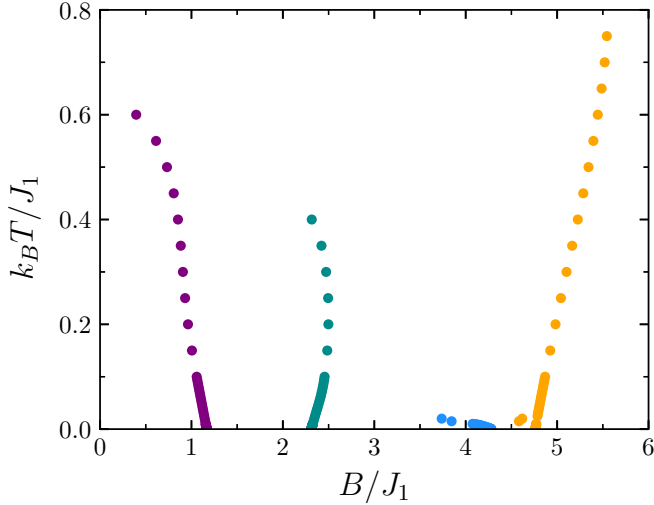


FIG. 9. Local maxima of $\partial\langle S_z \rangle / \partial B$ as a function of temperature T and magnetic field B for $C = 0.00638J_1$.

substantial changes in the resistance take place at the relative maxima of $\partial\langle S_z \rangle / \partial B$.

We note that the partition function

$$Z = \sum_{j=1}^{64} \exp\left(-\frac{E(j)}{k_B T}\right), \quad (9)$$

with $E(j)$ defined in Eq. (8) and Tables II and III is an analytic function of T and B from which all thermodynamic quantities can be derived.

In Fig. 9, we show the results for the local maxima of $\partial\langle S_z \rangle / \partial B$ as a function of temperature. As T is increased some local maxima disappear. In particular the transition at B_3 for $T = 0$ which involved a small change in $\langle S_z \rangle$ is rapidly blurred with increasing temperature (see Figs. 8 and 9). Since this is not experimentally the case, probably the nature of the third transition is different from that predicted by our model.

Another discrepancy with the experiment is that the last transition is displaced to larger B with increasing T in our theory. This is corrected when interoctahedra magnetic interactions are included (see next), since the effective field felt by each ion decreases with temperature.

1. Effects of magnetic interactions between different octahedra

The above picture is substantially modified when magnetic interactions of spins belonging to different octahedra are included. As it is well known, in a finite system there are no phase transitions, but the interoctahedra interactions, even if they are small, connect all Ce magnetic moments of the system. Even if these interactions are not known, one can conclude on general physical grounds, that the above described crossovers become real transitions if the magnetic space groups of the two phases involved are different. We have assumed here uniform magnetization in which all Ce spins have the same spin projection $\langle S_z \rangle / 6$, but the inter-octahedra interactions can modify this picture.

Looking at the irreducible representations of the point group of one octahedron (see Table II), one realizes that all

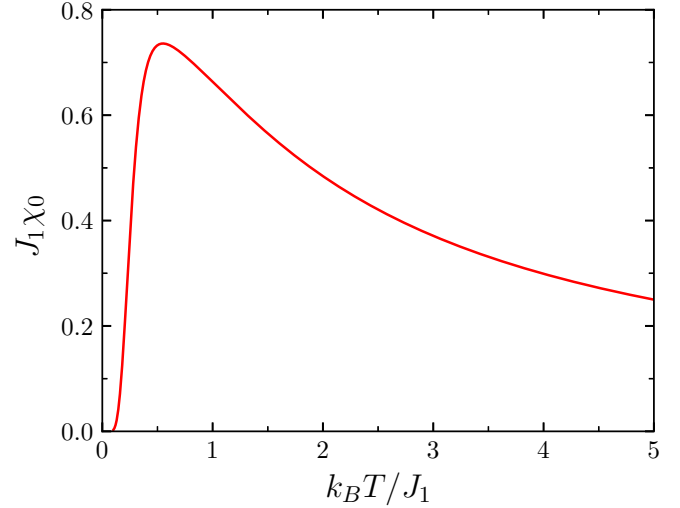


FIG. 10. Magnetic susceptibility as a function of temperature for $C = 0.00638J_1$.

jumps in the total spin of the octahedron induced by magnetic field at low temperatures are accompanied by a change of symmetry, except possibly for the jump between $S = 1$ and 2. For $S = 2$, the ground state has E_u symmetry and for $S = 1$ the ground state is degenerate between E_u and A_{1g} . However, as argued in Sec. IV E, the former is likely to be favored by the interactions between octahedra. Therefore it is possible that the second and third phases observed in Figs. 7 and 9 for increasing magnetic field at low temperatures correspond to the same magnetic group. Then one expects that at low temperatures one has a first-order transition but that it can end at a critical point at finite temperatures. This is consistent with the experimental observations in Fig. 7. For the rest of the transitions, one expects that they remain as real transitions for all finite temperatures, because of the different symmetries of the two phases involved.

E. Magnetic susceptibility as a function of temperature

In Fig. 10, we show the magnetic susceptibility defined as

$$\chi_0(T) = \left. \frac{\partial\langle S_z \rangle}{\partial B} \right|_{B=0}, \quad (10)$$

where the subscript 0 indicates that magnetic interactions between different octahedra have been neglected and only inter octahedra interactions have been taken into account. There is a maximum for $k_B T_{\max} = 0.5496J_1$ with $\chi_0(T_{\max}) = \chi_0^{\max} = 0.7360/J_1$. As it can be seen, the magnetic susceptibility is zero at low temperatures and the increase while increasing temperature is due to the population of excited triplet states. A further decrease in magnetic susceptibility occurs at even higher temperatures.

To discuss the effect of the magnetic interactions between different octahedra, let us assume that the effective magnetic field felt by each spin is increased including this interaction in mean field,

$$B_{\text{eff}} = B + K \frac{\langle S_z \rangle}{6}, \quad (11)$$

where K is the sum of the interactions felt by a given spin that are outside its octahedron, and it is assumed that the expectation value of all spins is the same ($\langle S_z \rangle / 6$) and point in the z direction. The ordering between different octahedra can be ferro- or antiferromagnetic, depending of which one minimizes the energy. Under these assumptions the magnetic susceptibility is

$$\begin{aligned} \chi &= \frac{\partial \langle S_z \rangle}{\partial B} = \frac{\partial \langle S_z \rangle}{\partial B_{\text{eff}}} \frac{\partial B_{\text{eff}}}{\partial B} \\ &= \chi_0 \left(1 + K \frac{\chi}{6} \right) = \frac{\chi_0}{1 - \frac{K}{6} \chi_0}. \end{aligned} \quad (12)$$

This implies that for a sufficiently large interaction $K > 6/\chi_0^{\text{max}}$, the system is magnetically stable in the range of temperatures for which $\chi_0(T) > K/6$, and there is a magnetizing transition at T_2 and demagnetizing transition at $T_1 > T_2$, where T_1 and T_2 are the two roots of $\chi_0(T) = K/6$. The identification of these two roots with T_{N_2} and T_{N_1} , respectively, opens the possibility for a temperature-driven transition from a nonmagnetic ground state to a weakly magnetic state at T_{N_2} , followed by a subsequent transition to another nonmagnetic state at T_{N_1} .

We have done calculations including this interaction, but it turns out that the required K is too large and shifts the B_i to too large values, which would require a gyromagnetic factor g much larger than expected.

We think that for the magnetic order, the hypothesis of a uniform magnetization of each octahedron is not correct, and that the system gains more energy for other distributions, for example with E_u symmetry, which is part of the ground state in the sector $S = 1$. Research along this line requires more information on the interactions, and breaking the O_h symmetry for the effective Hamiltonian of each octahedron.

More realistic interactions may transform nonmagnetic phases at finite temperatures into weakly magnetic ones. In any case, these findings align with the absence of distinct magnetic peaks in neutron diffraction experiments. In essence, under a zero magnetic field, the system likely exhibits characteristics akin to a valence-bond liquid, undergoing multiple magnetic transitions as the magnetic field strength increases, as previously described.

V. SUMMARY AND DISCUSSION

We have studied the compound $\text{Ce}_6\text{Ni}_6\text{P}_{17}$ based on a series of measurements (in powders and single crystals), which include magnetization, specific heat and resistivity. From the kinks in the susceptibility and resistivity, and the peaks in the

specific heat, a rich phase diagram in the plane of temperature T and magnetic field H is obtained, for $T < 1$ K and $H < 25$ kOe, where five different phases can be identified. Besides clear evidence of important magnetic fluctuations above the ordering temperatures is seen in all the physical properties measured, both on powder and single crystal $\text{Ce}_6\text{Ni}_6\text{P}_{17}$. The magnetic frustration originates on the Ce^{+3} magnetic ions which are accommodated on a highly frustrated crystal structure of body-centered cubic Ce_6 octahedrons.

From the entropy $\approx R \ln 2$ per Ce^{+3} ion at $T \sim 10$ K, one concludes that at low T the relevant degrees of freedom are Ce^{+3} doublets split by crystal field from the total angular momentum $J = 5/2$ of the $4f^1$ configuration. This fact suggests to use a spin-1/2 Heisenberg model including only the nearest-neighbor interaction J_1 as a first approximation to describe the system. The geometry corresponds to six spins at the vertices of a regular octahedron. We obtain that J_1 should be antiferromagnetic and since all faces of the octahedron are triangles, a perfect antiferromagnetic alignment is impossible and the system is highly frustrated. Nevertheless, the ground state has a rather simple structure [see Eqs. (5)–(7)] and is a singlet. For each octahedron as a function of increasing H the total spin in the model should jump gradually from $S = 0$ to 3. These jumps become crossovers at finite T , but in the real system, the magnetic interactions between different octahedra should lead to phases belonging to different magnetic space groups (except probably for the transition between $S = 1$ and 2) leading to magnetic transitions instead of crossovers.

Further progress in the understanding of the system would come from the identification of the ground state doublet of an isolated Ce^{+3} , as it would be an important step towards a detailed microscopic magnetic interactions model for the system. However our simple model is able to qualitatively account for most of the experimental evidence studied.

ACKNOWLEDGMENTS

The authors thank Bernardo Pentke for the SEM micrographs (Departamento Físicoquímica de Materiales CAB-CNEA). We are indebted to Julián Sereni for useful discussions. D. G. F. acknowledges financial support provided by Agencia I+D+i, Argentina, Grant No. PICT-2021-I-INVI-00852 and Universidad Nacional de Cuyo (SIIP) Grant No. 06/C018-T1. A. A. A. acknowledges financial support provided by PICT 2018-01546 and PICT 2020A-03661 of the Agencia I+D+i.

-
- [1] S. Doniach, *Physica B+C* **91**, 231 (1977).
 - [2] J. R. Iglesias, C. Lacroix, and B. Coqblin, *Phys. Rev. B* **56**, 11820 (1997).
 - [3] A. M. Lobos and A. A. Aligia, *Phys. Status Solidi C* **2**, 3564 (2005).
 - [4] F. Steglich, J. Aarts, C. D. Bredl, W. Liecke, D. Meschede, W. Franz, and H. Schafer, *Phys. Rev. Lett.* **43**, 1892 (1979).
 - [5] H. v. Löhneysen, A. Rosch, M. Vojta, and P. Wölfle, *Rev. Mod. Phys.* **79**, 1015 (2007).
 - [6] W. Zhou, C. Q. Xu, B. Li, R. Sankar, F. M. Zhang, B. Qian, C. Cao, J. H. Dai, J. Lu, W. X. Jiang, D. Qian, and X. Xu, *Phys. Rev. B* **97**, 195120 (2018).
 - [7] S. T. Bramwell and M. J. P. Gingras, *Science* **294**, 1495 (2001).
 - [8] L. Balents, *Nature (London)* **464**, 199 (2010).
 - [9] M. J. Harris, S. T. Bramwell, D. F. McMorrow, T. Zeiske, and K. W. Godfrey, *Phys. Rev. Lett.* **79**, 2554 (1997).
 - [10] S. T. Bramwell, S. R. Giblin, S. Calder, R. Aldus, D. Prabhakaran, and T. Fennell, *Nature (London)* **461**, 956 (2009).

- [11] J. Strečka, L. Čanová, M. Jaščur, and M. Hagiwara, *Phys. Rev. B* **78**, 024427 (2008).
- [12] A. Huq, J. F. Mitchell, H. Zheng, L. C. Chapon, P. G. Radaelli, K. S. Knight, and P. W. Stephens, *J. Solid State Chem.* **179**, 1136 (2006).
- [13] Y. Singh and P. Gegenwart, *Phys. Rev. B* **82**, 064412 (2010).
- [14] J. G. Sereni, M. Gomez Berisso, G. Schmerber, and J. P. Kappler, *Phys. Rev. B* **81**, 184429 (2010).
- [15] D. C. Johnston, R. J. McQueeney, B. Lake, A. Honecker, M. E. Zhitomirsky, R. Nath, Y. Furukawa, V. P. Antropov, and Y. Singh, *Phys. Rev. B* **84**, 094445 (2011).
- [16] P. A. Lee, *Science* **321**, 1306 (2008).
- [17] S. Lucas, K. Grube, C. L. Huang, A. Sakai, S. Wunderlich, E. L. Green, J. Wosnitza, V. Fritsch, P. Gegenwart, O. Stockert, and H. v. Löhneysen, *Phys. Rev. Lett.* **118**, 107204 (2017).
- [18] R. Oishi, Y. Ohmagari, Y. Kusanose, Y. Yamamen, K. Umeo, Y. Shimura, T. Onimaru, and T. Takabatake, *J. Phys. Soc. Jpn.* **89**, 104705 (2020).
- [19] S. R. Dunsiger, J. Lee, J. E. Sonier, and E. D. Mun, *Phys. Rev. B* **102**, 064405 (2020).
- [20] D. J. Braun and W. Jeitschko, *Acta Crystallogr., Sect. B* **34**, 2069 (1978).
- [21] N. Takeda, K. Izumi, H. Ono, S. Yodono, and T. Nakano, *J. Phys.: Conf. Ser.* **391**, 012071 (2012).
- [22] T. Koyama, H. Yamada, K. Ueda, T. Mito, Y. Aoyama, T. Nakano, and N. Takeda, *J. Phys.: Conf. Ser.* **683**, 012027 (2016).
- [23] J. Rodríguez-Carvajal, *Phys. B: Condens. Matter* **192**, 55 (1993).
- [24] G. M. Sheldrick, *Acta Cryst.* **C71**, 3 (2015).
- [25] K. Momma and F. Izumi, *J. Appl. Crystallogr.* **44**, 1272 (2011).
- [26] P. J. W. Moll, *Annu. Rev. Condens. Matter Phys.* **9**, 147 (2018).
- [27] See Supplemental Material at <http://link.aps.org/supplemental/10.1103/PhysRevB.109.054405> for a typical EDX spectra and Ce, Ni, and P distribution maps.
- [28] CCDC/FIZ Karlsruhe deposition service, <https://www.fiz-karlsruhe.de/en/produkte-und-dienstleistungen/das-kristallstrukturdepot>.
- [29] V. Fritsch, N. Bagrets, G. Goll, W. Kittler, M. J. Wolf, K. Grube, C. L. Huang, and H. v. Löhneysen, *Phys. Rev. B* **89**, 054416 (2014).
- [30] H. Zhao, J. Zhang, S. Hu, Y. Isikawa, J. Luo, F. Steglich, and P. Sun, *Phys. Rev. B* **94**, 235131 (2016).
- [31] M. S. Kim, M. C. Bennett, and M. C. Aronson, *Phys. Rev. B* **77**, 144425 (2008).
- [32] A. P. Ramirez, *Annu. Rev. Mater. Sci.* **24**, 453 (1994).
- [33] PPMS Heat Capacity Option User's Manual, 1085-150, Rev. L3 October, 2009
- [34] J. S. Hwang, K. J. Lin, and C. Tien, *Rev. Sci. Instrum.* **68**, 94 (1997).
- [35] J. C. Lashley, M. F. Hundley, A. Migliori, J. L. Sarrao, P. G. Pagliuso, T. W. Darling, M. Jaime, J. C. Cooley, W. L. Hults, L. Morales, D. J. Thoma, J. L. Smith, J. Boerio-Goates, B. F. Woodfield, G. R. Stewart, R. A. Fischer, and N. E. Phillips, *Cryogenics* **43**, 369 (2003).
- [36] L. J. D. Jongh and A. R. Miedema, *Adv. Phys.* **50**, 947 (2001).
- [37] N. Mufti, C. Klingner, L. Pedrero, M. Brando, K. Kaneko, C. Krellner, O. Stockert, and C. Geibel, *Phys. Status Solidi B* **247**, 743 (2010).
- [38] L. Pedrero, C. Klingner, C. Krellner, M. Brando, C. Geibel, and F. Steglich, *Phys. Rev. B* **84**, 224401 (2011).
- [39] A. Y. Kitaev, *Phys. Usp.* **44**, 131 (2001).
- [40] K. R. Lea, M. J. M. Leask, and W. P. Wolf, *J. Phys. Chem. Solids* **23**, 1381 (1962).
- [41] J. F. Cornwell, *Group Theory in Physics: An Introduction* (Academic Press, San Diego, London, 1997).